

Polarized emission from GaN/AlN quantum dots subject to uniaxial thermal interfacial stresses

O. Moshe and D. H. Rich^{a)}

Department of Physics and The Ilse Katz Institute for Nanoscale Science and Technology, Ben-Gurion University of the Negev, P.O. Box 653, Beer Sheva 84105, Israel

B. Damilano and J. Massies

Centre de Recherche sur l'Hétéro-Epitaxie et ses Applications, Centre National de la Recherche Scientifique, Rue B. Gregory, Sophia Antipolis, 06560 Valbonne, France

(Received 22 February 2010; accepted 3 May 2010; published 19 July 2010)

The authors have studied the excitation-dependent optical properties of GaN/AlN self-assembled quantum dots (QDs) grown on Si(111) substrates. Ensembles of QDs were subject to various external stress configurations that resulted from the thermal expansion coefficient mismatch between the GaN/AlN layers and the Si(111) substrate and ranged from in-plane uniaxial stress, primarily along the $\langle 11-20 \rangle$ directions, to in-plane biaxial stress, having magnitudes ranging from 15 to 30 kbars. The authors have exploited microcracks that form during the postgrowth cooling as stressors in order to create the highly localized regions of uniaxial stress over limited regions of the samples. Cathodoluminescence (CL) measurements of the excitonic transitions exhibit an in-plane linear polarization anisotropy in close proximity to microcracks that is strongly dependent on the e-beam current used to excite the QD ensemble. The excitonic transition energy in varying proximity to the microcracks was studied with CL wavelength imaging. Some aspects of the carrier recombination are inferred from the temperature dependence of the integrated CL intensity. CL activation energy (AE) imaging is used to study changes in the AE for the thermal quenching of the luminescence in close proximity to the microcracks, and correlations are obtained with changes in the QD excitonic transition energy and changes in the average AlN band edge energies relative to the ground electron and hole states in the QD. Localized CL spectroscopy of the QDs exhibits emissions from both the ground and excited states, whose relative contributions depend on the level of excitation and temperature. Experimental results indicate that the polarization anisotropy vanishes at high temperatures (~ 300 K) with an increasing excitation of the QDs, while the anisotropy decreases more slowly with excitation at low temperatures (~ 60 K). A theoretical modeling of the effect of carrier filling on the polarization anisotropy and the excitonic transition energy was performed, as based on three-dimensional self-consistent solutions of the Schrödinger and Poisson equations using the 6×6 $\mathbf{k} \cdot \mathbf{p}$ and effective mass methods for the calculation of the e - h wave functions. The authors attribute carrier filling and a thermal excitation of holes into higher energy QD hole states during excitation to account for the observed gradual decrease in the polarization anisotropy with an increasing electron-hole pair excitation density at $T=300$ K. © 2010 American Vacuum Society. [DOI: 10.1116/1.3435325]

I. INTRODUCTION

Group III-nitride-based wurtzite self-assembled quantum dots (QDs) have attracted much attention in the fundamental semiconductor physics and for potential device applications.¹⁻³ An important characteristic of group III-nitride compounds is the existence of a large polarization field, originating from both piezoelectric and pyroelectric polarizations. The charge polarization will create electric fields along the [0001] QD growth axis that will be screened in a complex manner when electrons and holes begin to fill the excited energy levels of the QD during sufficient levels of excitation.^{4,5} In this work, vertically stacked layers of GaN/AlN self-assembled QDs were grown by the Stranski-Krastanov method on a Si(111) substrate using molecular

beam epitaxy. During the subsequent cooling from growth temperatures, the thermal expansion coefficient mismatch between the Si substrate and the GaN/AlN film containing multiple layers of QDs leads to an additional tensile stress at the Si/III-nitride interface, which is partially relaxed by the formation of microcracks that propagate parallel to the interface and along the $\langle 11-20 \rangle$ directions.^{6,7} We have previously demonstrated that these defects serve as excellent stressors, which can modify the strain tensor of an ensemble of QDs in close proximity (i.e., within a few microns) of the microcracks.^{8,9} The excitonic luminescence of QDs with a uniaxial stress perturbation exhibits an in-plane linear polarization anisotropy.^{9,10}

In this study, we further explore the effects of localized stress perturbations in the GaN/AlN QD system by investigating the influence of excitation density and temperature on the measured polarization anisotropy. Using the method of

^{a)}Electronic mail: danrich@bgu.ac.il

cathodoluminescence (CL) imaging and spectroscopy, we excite locally groups or ensembles of vertically stacked QDs in varying proximity to the microcracks. We begin by using CL wavelength imaging (CLWI) to map the energy changes in the excitonic transition energy. The effects of screening of the polarization field in the QD, state-filling, changes in the polarization anisotropy with varying excitation, and thermal quenching of the QD luminescence were studied both experimentally and theoretically with a 6×6 $\mathbf{k} \cdot \mathbf{p}$ calculation method. The experimental results indicate that the polarization anisotropy vanishes at high temperatures with an increasing excitation of the QDs, while the anisotropy decreases more slowly with excitation at low temperatures. A theoretical modeling of the effect of carrier filling on the polarization anisotropy was performed, as based on three-dimensional (3D) self-consistent solutions of the Schrödinger and Poisson equations using the 6×6 $\mathbf{k} \cdot \mathbf{p}$ and effective mass methods for the calculation of the e - h wave functions, including the effects of the interfacial stress, microcrack-induced uniaxial stress perturbation, carrier-induced screening of the QD polarization field, sample temperature, and occupation of the QD excited states through changes in the electron and hole quasi-Fermi levels.

II. EXPERIMENT

The samples were grown by molecular beam epitaxy using the two-dimensional to 3D Stranski–Krastanov growth mode transition.^{2,11,12} Two samples were grown on Si(111) substrates and consist of AlN (30 nm)/GaN (400 nm)/AlN (700 nm) buffer layers followed by either 40 or 85 layers of GaN QDs, labeled as samples S40 and S85, respectively. The growth of sample S40 (S85) involved 18-nm- (6.7-nm-) thick AlN barrier layers with 2.6-nm- (1.6-nm-) thick GaN dot layers, resulting in an average dot height of ~ 5 nm (~ 3.7 nm), as determined previously by transmission electron microscopy (TEM) measurements for samples possessing very similar structures and growth conditions. Both samples were terminated with a 40-nm-thick AlN capping layer. The average dot density per QD plane is $\sim 5 \times 10^{11}$ cm^{-2} .

Our CL detection system is mounted on a JEOL 5910 scanning electron microscope (SEM). The samples were mounted on a variable temperature stage that is connected via a copper braid to a closed-cycle He cryorefrigerator. An ellipsoidal mirror with variable three-axis positioning collects luminescence emitted from the sample. The emitted luminescence is collected by the mirror and focused onto a coherent optical fiber bundle with a vacuum rotatable linear polarizer positioned before the fiber optics.⁹ Two polarization directions for the polarizer will be denoted with the subscripts \perp and \parallel to indicate detection orientations with \mathbf{E} perpendicular and parallel to a microcrack that is oriented along the [11-20] crystallographic direction. The polarization anisotropy ratio R_p is defined by the ratio of CL intensities I under two orthogonal polarizer orientations, and is given by $R_p = I_{\perp} / I_{\parallel}$. The light from the flexible fiber bundle was transferred to a 1/4 m monochromator outside the SEM vacuum

system. The spectral resolution of the monochromator was 2 nm (~ 15 meV) at $\lambda = 400$ nm (3.100 eV). The dispersed light was detected with a multi-alkali photomultiplier tube, which enabled photon counting. Time-resolved CL experiments were performed with the method of delayed coincidence in an inverted single photon counting mode.¹³ Electron beam pulses of 50 ns width with a 1 MHz repetition rate were used to excite the sample.

We employed CLWI to enable a spatial mapping of the peak energy of the emission from the ensemble of GaN QDs. CLWI is accomplished by acquiring a series of 50 discrete monochromatic images, constructing a local spectrum at all 640×480 scan points within the image, and determining the excitonic transition energy $E_x(x, y)$ at which there is a peak in the CL spectrum at each scan point (x, y) .¹⁴ Activation energy (AE) images likewise are obtained by measuring the change in the CL intensity versus temperature for each point (x, y) , determining the local AE for the thermal quenching of the luminescence at each point by a least-squares fit in the $240 \leq T \leq 300$ K temperature range, and plotting a gray scale intensity map that represents the AE.¹⁵

III. THEORETICAL CALCULATIONS USING A THREE-DIMENSIONAL $\mathbf{K} \cdot \mathbf{P}$ METHOD

The electron and hole wave functions and energies were obtained with 3D 6×6 $\mathbf{k} \cdot \mathbf{p}$ calculations using the NEXTNANO³ quantum nanostructure simulation code.^{8,9,16} The calculations utilized a 3D Schrödinger equation for wurtzite materials including strain, deformation potentials, spin orbit coupling, and piezo- and pyroelectric charges, the latter of which accounts for the large polarization field in the QD along the [0001] growth direction. In order to calculate the wave functions, a single band model for the electrons and a six-band $\mathbf{k} \cdot \mathbf{p}$ Hamiltonian for the holes were employed. The coupling between the conduction and valence bands was neglected, owing to the size of the GaN and AlN bandgaps.¹⁷

We employed the material parameters used previously for calculations of the polarization field and eigenstates in GaN/AlN QDs.^{18–20} The fully strained GaN/AlN QDs were simulated by minimization of the elastic energy within a continuum model approach that takes into account the symmetry of the hexagonal crystal structure. We employed a simulated region size of $19 \times 19 \times 22$ nm^3 containing a single pyramidal QD with a typical discretized grid of $60 \times 70 \times 112$ nodes for calculations of the strain minimization, Pikus–Bir, $\mathbf{k} \cdot \mathbf{p}$, and single band effective mass Hamiltonians. External tensile stresses ranging from purely biaxial to uniaxial were used to simulate the thermal stress in the AlN barrier layers in varying proximity to the microcracks.

We have extended the multiband $\mathbf{k} \cdot \mathbf{p}$ and single band effective mass treatments for the occupation of multielectron and -hole states. Self-consistent calculations of the Schrödinger and Poisson equations using the 6×6 $\mathbf{k} \cdot \mathbf{p}$ and effective mass methods for the calculation of the e - h wave functions in the Hartree approximation were performed. The primary multicarrier correction to the energy levels results from the carrier-induced screening of the electric field in the

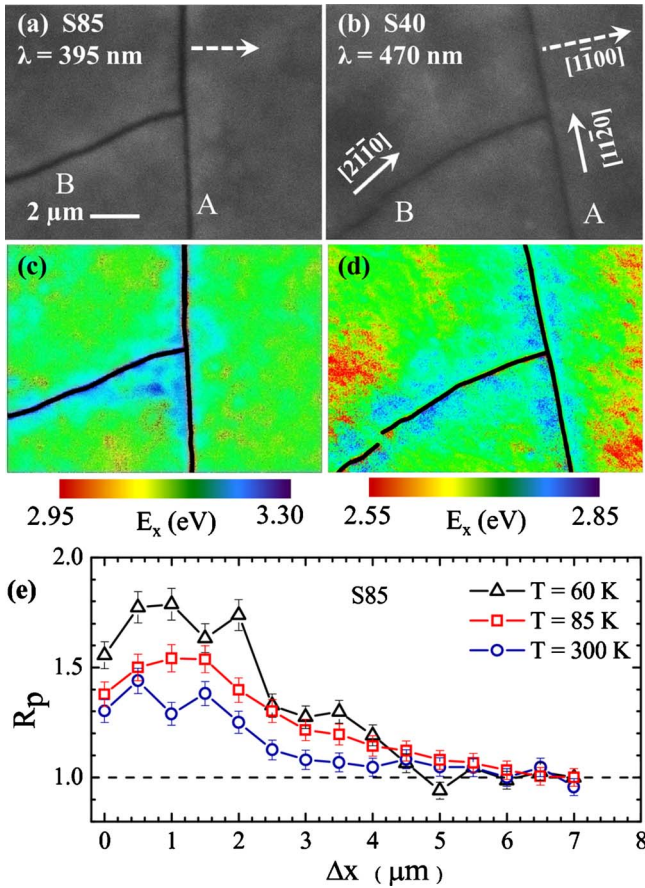


FIG. 1. (Color online) Monochromatic CL images acquired with $E_b = 15$ keV and $I_b = 200$ pA of samples S85 and S40 in (a) and (b), respectively. CL wavelength images, which map the excitonic transition energy E_x , are shown in (c) and (d) for samples S85 and S40. The color bars show the false-color mapping into the transition energy (E_x), while the microcrack regions are shown in black. The polarization anisotropy ratio $R_p = I_{\perp}/I_{\parallel}$ vs distance Δx from a microcrack for S85 is shown in (e) for three temperatures.

QD, which is caused by piezoelectric and pyroelectric polarizations. Our approach included the effects of the interfacial stress, the microcrack-induced uniaxial stress perturbation, carrier-induced screening of the QD polarization field, temperature, and occupation of the QD excited states through changes in the electron and hole quasi-Fermi levels, φ_e and φ_h .

IV. EXPERIMENTAL RESULTS AND DISCUSSION

A. Monochromatic CL and CL wavelength imaging

Monochromatic CL images for samples S85 and S40 were acquired for detection wavelengths of 395 and 470 nm, respectively, as shown in Figs. 1(a) and 1(b). The electron beam current and energy were, respectively, $I_b = 200$ pA and $E_b = 15$ keV, and the samples were maintained at a temperature of 300 K. In previous measurements and modeling of these samples, we obtained biaxial and uniaxial tensile stress values of ~ 30 and ~ 15 kbars at room temperature for samples S85 and S40, respectively.^{8,9} We chose locations on

both samples that revealed the intersection of microcracks and formation of a junction in each image. The near vertically oriented microcracks labeled A in Figs. 1(a) and 1(b) are oriented along the $[11\bar{2}0]$ directions and indicate cracks that propagated in a linear fashion. The intersecting microcrack labeled B in each image appears to have propagated with rougher segments, shorter lengths, and some jagged edges that have led to deviations from a pure $[2\bar{1}\bar{1}0]$ direction and intersects with the vertical crack at an angle of $\sim 90^\circ$, the $[1\bar{1}00]$ direction. The effective spatial resolution in CL for these imaging conditions is ~ 0.3 μm . We observed the presence of smaller microcracks in the SEM images whose features are barely visible in the corresponding CL images. The smaller cracks may represent an incomplete severing of the film and thus will have a reduced effect on the optical properties.

CLWI of samples S40 and S85 is shown in Figs. 1(c) and 1(d) in the identical regions that correspond to the monochromatic images of Figs. 1(a) and 1(b). The false-color images represent peak CL spectral energies $E_x(x, y)$, which exhibited maximum local variations of ~ 200 meV, as mapped by the color bars below each image. The largest transition energies of ~ 3.20 and 2.75 eV are observed in close proximity (within ~ 1 μm) of the microcracks, whereas the smallest are observed at ~ 3.05 and ~ 2.65 eV at distances larger than ~ 5 μm from the microcracks for samples S85 and S40, respectively. As will be demonstrated below, the average energy shifts as determined by a line scan analysis are much smaller than the maximum fluctuations and lead to average blueshifts of ~ 80 and 50 meV for S85 and S40, respectively, in transitioning between the biaxially and uniaxially stressed regions. Deviations between these maximum and spatially averaged fluctuations are attributed to the presence of threading dislocations with their characteristic strain fields, inhomogeneities during growth that can lead to an anisotropic thermal strain upon cooling, and the presence of smaller microcracks with narrow gaps, which are more difficult to detect with CL and SEM imaging.

B. Polarized CL line scan measurements

We have examined in detail the dependence of R_p ($R_p = I_{\perp}/I_{\parallel}$) as a function of distance (Δx) from a microcrack, as shown in Fig. 1(e) for sample S85. It is clear that R_p decreases monotonically toward $R_p = 1$ as the e-beam is positioned at distances (Δx) sufficiently far from the microcracks ($\Delta x > \sim 5$ μm), for the various temperatures shown. Again, the maximum value of R_p occurs for the lowest temperature, and this value decreases as the temperature increases. An increased uniaxial tensile stress near the microcrack and an increased biaxial tensile stress far from the microcrack are expected to occur as the temperature is reduced leading to an increased value of the polarization anisotropy at lower temperatures. The polarization anisotropy ratio R_p is a direct probe of deviations from biaxial symmetry.^{9,10} Previously, we have also examined the spatial range W_R over which R_p deviates from unity and its temperature dependence.¹⁰

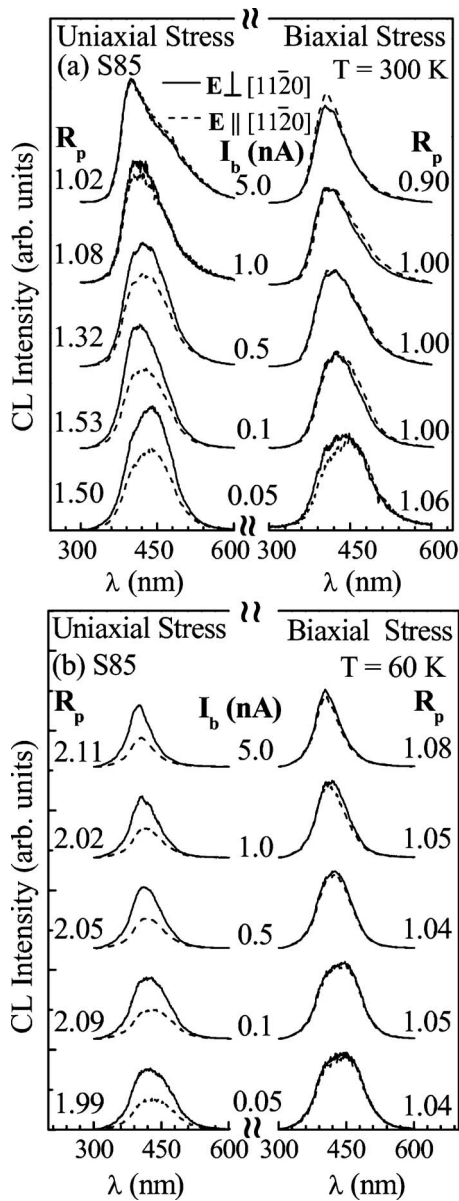


Fig. 2. Stack plots of CL spectra of sample S85 acquired with polarization detection orientations of $E \perp [11\bar{2}0]$ and $E \parallel [11\bar{2}0]$ (perpendicular and parallel to a microcrack direction) for e-beam currents I_b ranging from 50 pA to 5 nA. The CL spectra were acquired with the e-beam focused in regions of pure uniaxial tensile stress and pure biaxial tensile stress, which were located at distances Δx of 0.5 and 5 μm , respectively, from the microcrack. Sets of spectra are shown for $T=300$ K and $T=60$ K, in (a) and (b), respectively. The polarization anisotropy ratio $R_p = I_{\perp}/I_{\parallel}$ is indicated for each set of CL spectra acquired with e-beam currents, as shown.

C. Excitation-dependent polarized CL spectroscopy

We have performed excitation-dependent local CL spectroscopy measurements by positioning the e-beam at various points along the $[1\bar{1}00]$ direction [dashed white line in Fig. 1(a)]. Stack plots of local CL spectra for sample S85 are shown in Fig. 2 for temperatures (T) of 300 and 60 K and for positions Δx of 0.5 and 5 μm , which represent regions of nearly pure uniaxial and biaxial tensile stresses, respectively, as labeled in the panels of Fig. 2. For regions of uniaxial stress ($\Delta x=0.5$ μm), Fig. 2 shows that R_p increases from

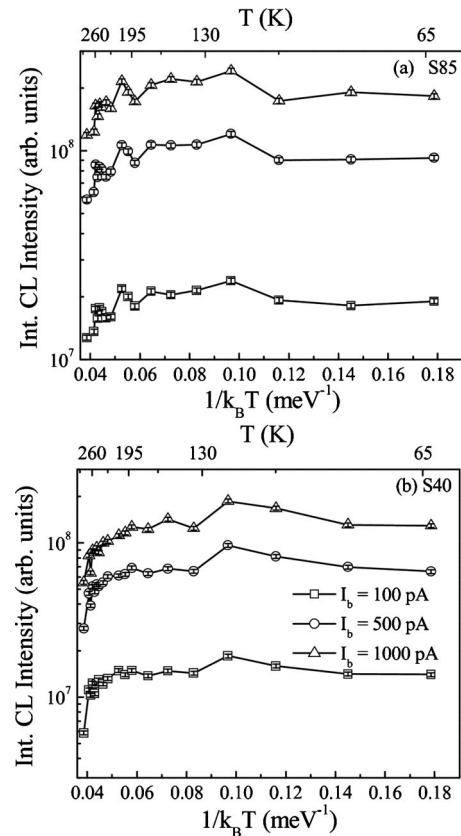


Fig. 3. Integrated CL intensity of the QD excitonic peak vs $1/k_B T$ for samples S85 (a) and S40 (b). The measurements were performed for e-beam currents I_b of 100, 500, and 1000 pA. Error bars for the intensities are shown inside the open symbols.

~ 1.5 to ~ 2.1 as the temperature decreases from 300 to 60 K for sample S85. For the region where biaxial stress is predominant ($\Delta x=5$ μm), R_p does not deviate too far from 1. The maximum deviation of $\sim 10\%$ may reflect the presence of defects as previously explained. CL spectra were acquired for e-beam currents I_b ranging from 50 pA to 5 nA. Of particular relevance is the large excitation dependence of R_p that is observed for $T=300$ K in Fig. 2(a) and yet strikingly absent in the measurements for $T=60$ K, as shown in Fig. 2(b). For $T=300$ K, R_p is observed to decrease from 1.5 to ~ 1.0 as the e-beam current increases from 50 pA to 5 nA, while $R_p \approx 2.0$ and nearly constant over the same range of excitation for $T=60$ K. Such a dependence on the excitation and temperature will be explained in the context of the thermal excitation of holes into higher energy QD hole states possessing partially orthogonal p -orbital characters in the discussion on theoretical modeling in Sec. IV G. As expected, for the regions of biaxial stress, R_p remains approximately 1 and independent of temperature and excitation, due to the biaxial symmetry.

D. Activation energy for the thermal quenching of the luminescence

We have further examined the integrated CL intensity as a function of temperature, as shown in Fig. 3. The CL inte-

grated intensity was measured without polarization detection. The behavior shows that in general the CL intensity increases as the temperature is lowered from 300 to ~ 200 K. For temperatures lower than 200 K small fluctuations are observed in the intensity before a maximum is found at 120 K, followed by an $\sim 15\%$ – 20% decrease as temperature is further reduced to 70 K. The CL intensity variation with temperature appears to be similar for both samples and occurs similarly for the three beam currents I_b of 100, 500, and 1000 pA used to excite the samples. Moreover, the error due to random fluctuations in the measured CL intensity for each of the curves in Fig. 3 is observed to be $\sim \pm 3\%$ of the integrated CL intensity and is shown contained in each of the open data symbols of the figure. The random error is evidently much smaller than variations due to temperature-dependent changes in the carrier collection and luminescence efficiency of the QDs. The consistency in this behavior for the three excitation conditions suggests that the carrier dynamics is affected in subtle ways by a further reduction in temperature for $T < 120$ K. The injection of the high energy e-beam involves the excitation of excess carriers, followed by thermalization in the AlN barriers, and subsequent collection in the wetting layer and finally into the GaN QDs. The initial increase in the CL intensity in Fig. 3 as the temperature is reduced from room temperature is due to a partial quenching of nonradiative defect channels in the barrier. As the temperature is further lowered the aforementioned small fluctuations occur in the range $225 > T > 175$ K in both samples, revealing that potential fluctuations in the barrier regions surrounding the QD will begin to likely impede the process of carrier collection in the QD as the temperature is lowered in this range. Finally, the peak of the CL intensity at $T = 120$ K, followed by a decrease in intensity, suggests that carrier collection is reduced due to the absence of sufficient thermal energy to overcome certain small potential barriers for these particular carrier collection pathways.

By examining the change in the integrated QD excitonic emission intensity, $I(T)$, as a function of temperature, the activation energy (E_A) for the thermal quenching of luminescence near room temperature can be determined from the slopes of the Arrhenius semilog plots using $I(T) = I_0 \exp(E_A/k_B T)$.^{8,21} CL AE images of both samples are shown in Fig. 4. The images were obtained by measuring the integrated CL intensity in the $240 \text{ K} \leq T \leq 300 \text{ K}$ range and determining the AE for the thermal quenching of the luminescence at each of the 640×480 raster scan points in the images by a linear least-squares fitting. It is apparent from the images that most activation energies range from 20 to 80 meV, with the largest activation energies being localized in close proximity to the microcracks.

Thermal activation generally reflects the thermal energy required to remove confined carriers over a barrier before they can recombine radiatively. The change in E_A is thus likely connected to stress-induced changes in the AlN conduction and valence band edges relative to the ground state e - h levels in the QD (i.e., $\Delta E_{c,e}$ and $\Delta E_{v,h}$), as a reduced tensile stress near the microcracks will lead to an increased

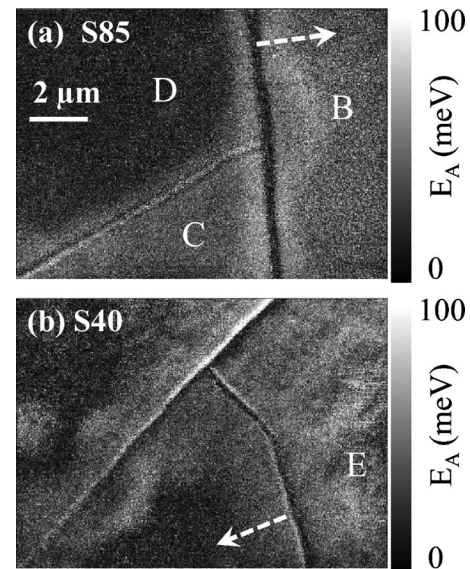


FIG. 4. AE images are shown in a gray scale for samples S85 (a) and S40 (b). The images were acquired for the temperature range of $240 \leq T \leq 300$ K. The gray scale bar shows the mapping of the activation energy E_A for the thermal quenching of the luminescence. The AE images are observed to be sensitive to the stress contours and to various defects and inhomogeneities. The dashed lines with arrows indicate regions in which line scans of the AE were constructed.

AlN bandgap energy.⁸ $\Delta E_{c,e}$ and $\Delta E_{v,h}$ are defined as the energy differences between the AlN conduction and valence band edges and the QD ground state electron and hole levels, respectively. Thus, changes in E_A are expected to correlate with the stress-induced changes in the band edges and should serve as a sensitive probe of the strain fields in varying proximity to the microcracks, dislocations, and sample inhomogeneities. The gray scale contrast shown in the AE images of Fig. 4 reveals the stress contours around the microcracks. The junction formed by the intersection of two microcracks shows a bulge in the stress contour, labeled as B in Fig. 4(a). A larger tensile stress relaxation has led to extended regions of an increased AlN bandgap near the junction, causing a protrusion in the distribution of larger E_A in this region. The lower triangular region formed by the intersection of the two cracks (labeled C in the figure) also shows a larger average E_A that is likely caused by a reduced tensile stress relative to the regions above the triangle, labeled D. Region D is presumably subject to a higher tensile stress due to the obtuse angle of the crack intersection in this region. An area that exhibits a higher density of defects, including smaller microcracks that are apparent as narrow white whiskers, is observed in the region labeled as E in Fig. 4(b). A larger average E_A in this region appears consistent with a defect-induced reduction in the average thermal tensile stress.

E. Line scan analysis of activation energy, excitonic transition energy, and band edge energy

A line scan analysis of E_A and E_x is shown in Fig. 5. The excitonic transition energy increases by ~ 50 and 80 meV, for samples S40 and S85, respectively, in transitioning from bi-

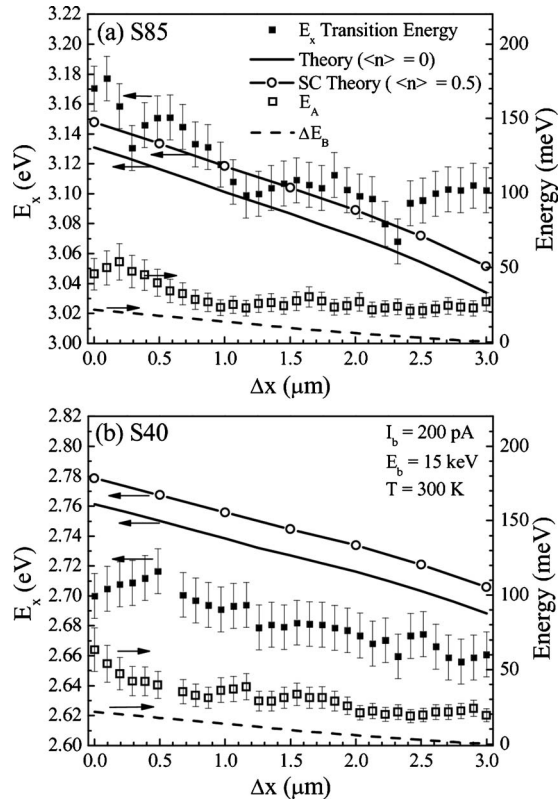


FIG. 5. Line scan analysis for samples S85 (a) and S40 (b) showing the measured excitonic transition energy E_x and activation energy E_A obtained from scans along the dashed lines in Figs. 1 and 4. The theoretical SC calculation of E_x vs distance is shown for the cases of $\langle n \rangle = 0.5$ and $\langle n \rangle = 0$ (solid lines). The calculated changes in the average band edge energy relative to the ground electron and hole states of the QD, $E_B = (\Delta E_{c,e} + \Delta E_{v,h})/2$, are shown (dashed lines). The change in E_B is referenced relative to the biaxial region in which $\Delta E_B = 0$. For the structure of S40, the calculated E_x curves have been offset downward by 110 meV to facilitate a comparison with the experimental E_x data.

axial to uniaxial stress near the cracks, while E_A increases from ~ 20 to ~ 50 meV in both samples for the particular regions identified by the dashed lines in Fig. 4. The calculated transition energy E_x vs Δx is also shown in Fig. 5 for both samples. The calculation was performed self-consistently, assuming an electron/hole occupancy of $\langle n \rangle = 1/2$, which is the occupation used to calculate transition energies in Slater's transition state for ground state optical transitions.^{22,23} We have included a constant Coulomb energy of 90 meV, which is obtained from a previous 3D $\mathbf{k} \cdot \mathbf{p}$ calculation.²⁴ The theory curves for E_x in Fig. 5 show a calculated transition energy increase of ~ 75 and 95 meV for the structures of S40 and S85, respectively, in transitioning from biaxial to uniaxial stress over the 3 μm region shown. Although the calculated values for the blueshifts of E_x over this transition region are greater than the experimental values by ~ 25 meV for S40 and ~ 15 meV for S85, these results represent a reasonable agreement between experiment and theory when considering the large full widths at half maximum (FWHMs) of ~ 490 and ~ 650 meV for the CL spectral lineshapes of the broadened QD ensembles for S40 and S85, respectively, as observed in Fig. 2 for S85. Deviations

between the experimental and calculated values of E_x are related to the choice of QD size, aspect ratio, and estimation of the stress values.^{8,9} Nevertheless, the average energy shifts ΔE_x for the calculated and experimental values of E_x in transitioning from the biaxially stressed region to the uniaxially stressed region are similar in magnitude and direction for the structures of S40 and S85 in Fig. 5, thereby illustrating that the model correctly evaluates the strain-induced changes in the transition energy.

Since the change in stress tensor, when moving from regions of biaxial stress (greater than $\sim 3 \mu\text{m}$ from the cracks) to uniaxial stress very near the crack, results in corresponding changes in $\Delta E_{c,e}$ and $\Delta E_{v,h}$, we plot the average change in the average band edge energy difference ΔE_B , where $E_B = (\Delta E_{c,e} + \Delta E_{v,h})/2$, as a function of distance from the crack in Fig. 5 to compare with the change in the activation energy ΔE_A , referenced to the biaxially stressed regions far from the microcracks. The AlN conduction and valence band edge energies relative to ground state electron and hole levels are determined from the $6 \times 6 \mathbf{k} \cdot \mathbf{p}$ calculations for the AlN tensile stress configurations that ranged continuously from biaxial to uniaxial. The electron and hole energy states were calculated self-consistently (SC), assuming half occupied electron and hole levels (i.e., $\langle n \rangle = 1/2$). For comparison a non-SC calculation (i.e., $\langle n \rangle = 0$) is shown alongside the curve for $\langle n \rangle = 1/2$. It is worth noting that the average transition energy E_x for $\langle n \rangle = 1/2$ is blueshifted by ~ 17 meV relative to the case for $\langle n \rangle = 0$ for both structures, S40 and S85. A strong correspondence in behavior between ΔE_B and ΔE_A versus distance from the microcrack is demonstrated in Fig. 5. This further supports our initial hypothesis that changes in the thermal activation are associated with changes in the AlN barrier band edges relative to the QD $e-h$ levels, owing to deep level defects in the AlN matrix that are responsible for the thermal quenching of the luminescence.⁸ Moreover, the agreement between the values of the change in band edge and activation energies (i.e., $\Delta E_B \approx \Delta E_A \approx 30$ meV) suggests that the process of thermal re-emission from the ground exciton states to the defect states in the barrier involve correlated $e-h$ pairs. If carriers are re-emitted as correlated $e-h$ pairs, then according to the requirement of detailed balance the measured activation energy would be about half of the total barrier height for nonradiative recombination.^{21,25} Therefore, in transitioning from biaxial stress to uniaxial stress over the range $\Delta x \approx 3 \mu\text{m}$, the relation $\Delta E_B \approx \Delta E_A$ is consistent with the thermal activation of correlated $e-h$ pairs. Otherwise, the re-emission of excitons would require $\Delta E_A \approx 2\Delta E_B$ (i.e., the activation energy should correspond to the total barrier height).²⁵ Our assumption again in this analysis is that the defect states close to the GaN/AlN QD interfaces are tied to the AlN conduction and valence band edges.

Other salient aspects of the calculations are shown in Fig. 6, in which E_x is plotted versus stress for the cases of pure uniaxial and biaxial tensile stresses (σ_{yy}) for both samples. While the exciton transition energy E_x is sensitive to the volume and aspect ratio of the QD, the energy shift ΔE_x

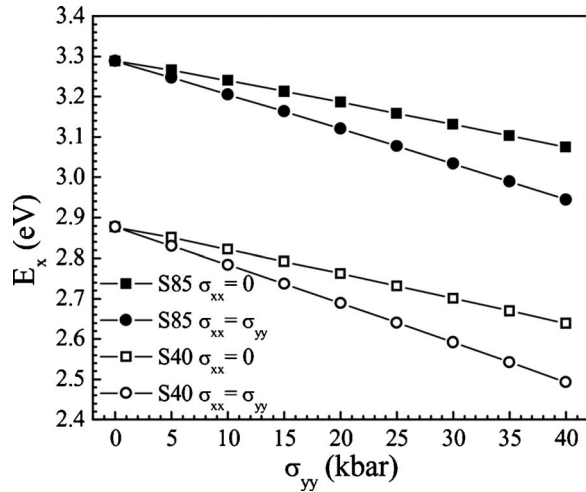


FIG. 6. Calculated excitonic transition energy E_x for samples S85 and S40 for the cases of pure uniaxial and biaxial tensile stresses, as a function of the stress component σ_{yy} .

between pure uniaxial and biaxial stresses primarily depends on the magnitude of the stress. The calculations show that energy shifts ΔE_x of ~ 50 and ~ 80 meV for S40 and S85 (from Figs. 1 and 5) correspond to stresses of ~ 20 and ~ 30 kbars, consistent with values obtained in our previous studies.^{8–10}

F. Excitation dependence of the CL peak energies and calculated electron and hole quasi-Fermi levels

We have employed a standard approach that determines the relationship between the average $e-h$ occupancy in the QD $\langle n \rangle$ and the electron beam current I_b .²⁶ Time-resolved CL was carried out to measure the carrier lifetime τ as a function of I_b for each sample. In Fig. 7, we show the measured

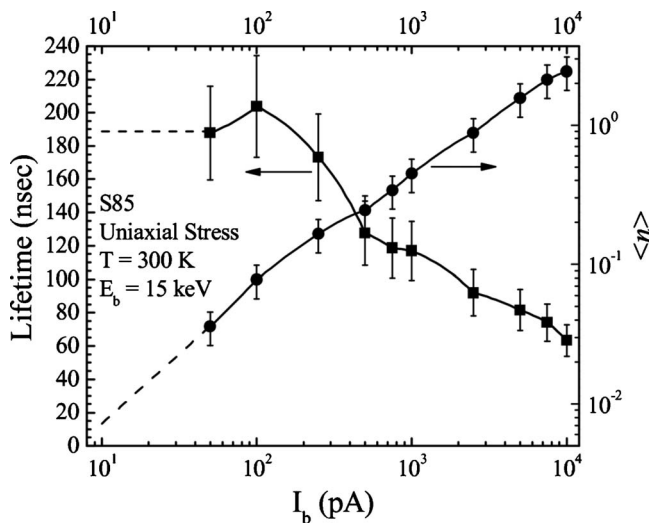


FIG. 7. Measured lifetime τ and average occupation number $\langle n \rangle$ for various e-beam injection currents I_b . The relation described in Ref. 26 was used to connect $\langle n \rangle$ with I_b . The dashed lines represent interpolated values for τ and $\langle n \rangle$. The dashed lines show an extrapolation for values not measured.

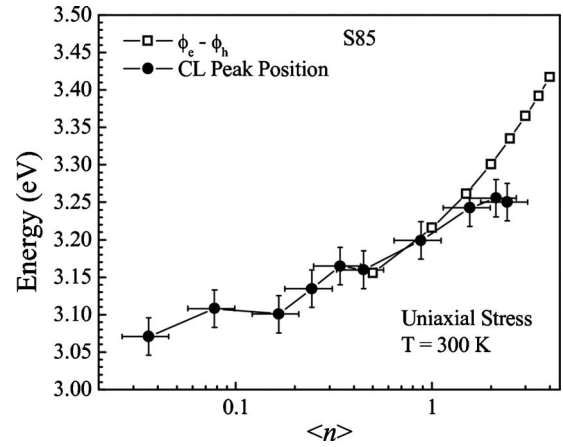


FIG. 8. Measured CL peak QD transition energy and the calculated difference in the QD electron and hole quasi-Fermi levels, $\varphi_e - \varphi_h$, as a function of average state occupancy $\langle n \rangle$. The relation between $\langle n \rangle$ and I_b is shown in Fig. 7.

lifetime and $\langle n \rangle$ as a function of I_b for S85. The results for the self-consistent calculations for varying excitation conditions are shown in Fig. 8 for the S85 structure. We show the calculated difference in quasi-Fermi levels $\varphi_e - \varphi_h$ as a function of $\langle n \rangle$ at $T=300$ K. The experimental energy positions of the peaks of the CL spectra for various electron-hole occupation $\langle n \rangle$ for sample S85, as calculated from the method of Ref. 26, are shown in Fig. 8 for comparison. As the quasi-Fermi levels represent the approximate energy positions of the highest electron and hole levels that participate in excitonic transition, their difference should then account for changes in these energy states due to the screening of the polarization field of the QD. Changes in $\varphi_e - \varphi_h$ with $\langle n \rangle$ should also reflect the energy shifts in E_x , associated with changes in the e-beam current I_b . For the most part, the energy values and the slopes of the experimental E_x and theoretical $\varphi_e - \varphi_h$ are in approximate agreement for both samples. Deviations between experiment and theory, and some experimental fluctuations are attributed to a nonuniform filling of the QDs owing to inhomogeneities in the excitation volume of the e-beam and the subsequent diffusion of carriers before collection into the QDs.

G. Theoretical calculations and analysis of the excitation dependence of the polarization anisotropy

Spatial variations in the optical polarization properties are attributed to stress-dependent variations in the p_x and p_y characters of the valence band edges and the ground state hole wave function. Previously, we showed that a change from biaxial to uniaxial stress alters the admixture of p_x and p_y characters of the band edges and ground state hole wave function, changes the shape and direction of elongation of the hole isosurfaces, and accounts well for the subsequent anisotropy in the *ground state* polarization dependent optical transitions and its spatial variation in the vicinity of the microcracks.⁹ We have extended this analysis in the present article to understand the excitation-dependent polarized CL

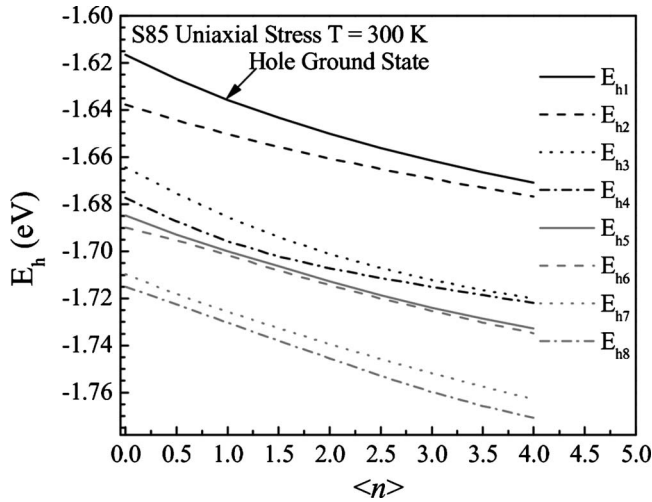


FIG. 9. Calculated hole energy levels vs state occupancy $\langle n \rangle$ for the structure of S85 for the first eight hole energy levels for $T=300$ K. The calculations were performed for the case of pure uniaxial stress. The collective downward shift in energy is due to the screening of the QD electric field caused by filling of the electron and hole states through the state occupancy $\langle n \rangle$. The calculations were performed self-consistently and holes were arranged among the states according to Fermi–Dirac statistics.

results of Fig. 2 for sample S85. These results show that the polarization anisotropy ratio R_p decreases from 1.50 to 1.02 as the beam current increases from 50 pA to 5 nA for $T=300$ K in close proximity to the microcrack (i.e., a position of uniaxial stress). A striking contrast to this behavior is observed for $T=60$ K, in which $R_p \approx 2$ and constant over for the same uniaxial stress region. Moreover, the data of Fig. 7 show that for $10 \text{ pA} \leq I_b \leq 10 \text{ nA}$, the average e - h occupancy varies from $\sim 0.01 \leq \langle n \rangle \leq \sim 3$ for S85.

The striking difference in the temperature-dependent behavior of R_p suggests that thermal excitation to higher lying hole states plays an important role in reducing R_p for higher excitation conditions at room temperature. Since the energy spacing between confined electron states is approximately four to five times greater than the spacing for hole states, which have spacings typically ranging from 10 to 20 meV, we hypothesize that the thermal excitation for holes near $T=300$ K will have an appreciable effect on the distribution of hole occupancy, particularly for high excitation conditions (i.e., $\langle n \rangle > \sim 1$). We have calculated self-consistently the spectrum of hole states using the 3D 6×6 $\mathbf{k} \cdot \mathbf{p}$ method, as previously discussed. The energies of the hole states E_{hi} , where i indicates the i th confined hole level, are shown as a function of the average occupation number $\langle n \rangle$ in Fig. 9. As expected, the spectrum of hole states shifts downwards in energy an average rate of ~ 15 meV per addition of an e - h pair due to the partial screening of the electric field in the QD. A similar upward shift of ~ 8 meV per e - h pair for electron levels also occurs, resulting in a net shift of the transition energy E_x that is ~ 23 meV per e - h pair for S85, which is similar to changes observed in previous CL measurements.²⁷ These energy shifts are obtained by averaging over the values obtained for $\langle n \rangle$ ranging from 0.5 to 4.

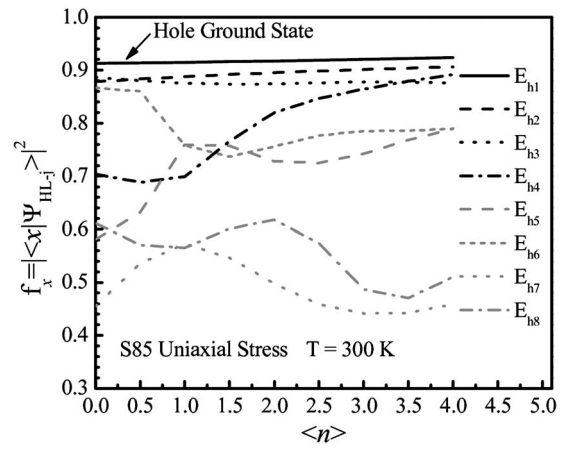


FIG. 10. Relative p_x -orbital character of the Bloch states $f_{xj} = |\langle x | \psi_{hj} \rangle|^2$ is shown as a function of average state occupancy $\langle n \rangle$. The calculations were performed self-consistently for the first eight hole energy levels (i.e., $j = 1-8$). The calculations were performed for the case of pure uniaxial stress. As expected, f_{xj} generally decreases as the state number j increases.

We note that differences in the average energy shift between the electron and hole states are due to differences in confinement and localization for both particles.

It is possible to observe the position and stress-dependent character of the wave function by projecting the three Bloch states with like spins, $|x\rangle$, $|y\rangle$, and $|z\rangle$, onto the hole wave function by calculating $f_{wFi} = |\langle i | \psi_h \rangle|^2$ where $i=x, y$, and z . We note that y is referenced as the $[11-20]$ microcrack direction in the calculations. We show $f_{xj} = |\langle x | \psi_{hj} \rangle|^2$ for the lowest eight hole states as a function of the e - h occupation number $\langle n \rangle$ in Fig. 10. The relative p_x -orbital character of the Bloch states f_{xj} reduces dramatically for higher energy hole states (i.e., for $j \geq 2$) and is a function of $\langle n \rangle$. Thus, we expect that the polarization anisotropy ratio R_p will decrease for optical transitions that involve increasingly higher energy hole states, as obtained by increasing excitation $\langle n \rangle$ or an enhanced thermal excitation to higher energy hole states for $T=300$ K. Using the spectrum of hole wave functions that were calculated self-consistently, we have calculated R_p at high and low temperatures (300 and 5 K) by taking into account the occupation of the excited holes using Fermi–Dirac statistics in a fully self-consistent fashion involving separate electron and hole occupation numbers, n_i^e and n_i^h . The integrated intensity of polarized luminescence is determined by the carrier occupation in the QD and the electron-hole wave function overlap according to

$$I_{\perp, \parallel} = \sum_{i,j} n_i^e n_j^h |M_{\perp, \parallel}^{(i,j)}(n_i^e, n_j^h)|^2,$$

where

$$M_{\perp, \parallel}^{(k,l)}(n_k^e, n_l^h) = \sum_{j=1}^2 \sum_{i=1}^6 \int d^3r F_{ek,j}^*(\vec{r}) F_{hl,i}(\vec{r}) \langle j | \hat{e}_{\perp, \parallel} \cdot \frac{\hbar}{i} \vec{\nabla} | i \rangle. \quad (1)$$

The Bloch part of the electron wave function $|\psi_e\rangle$ is represented by two basis s -like states $|\mathbf{S}\uparrow\rangle$ and $|\mathbf{S}\downarrow\rangle$ and denoted

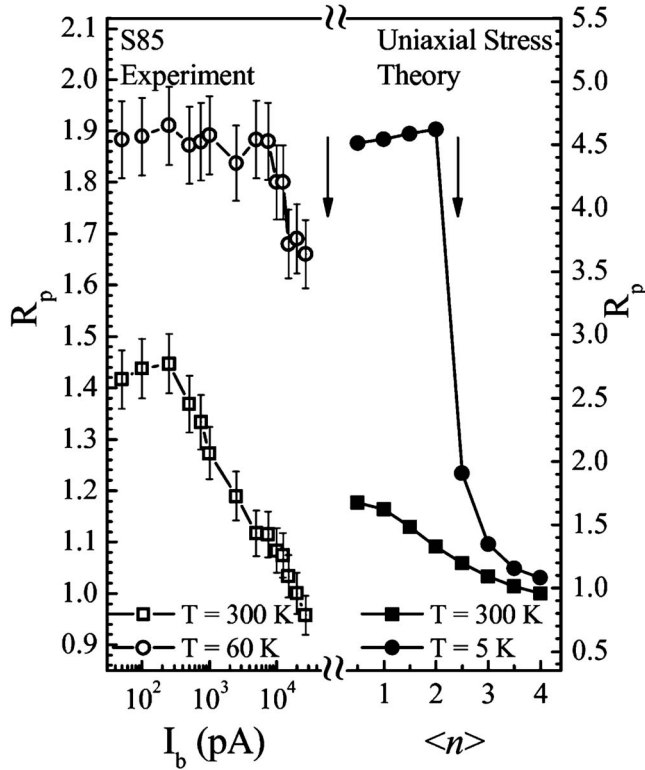


FIG. 11. Calculated and experimental polarization anisotropy ratio $R_p = I_{\perp}/I_{\parallel}$ vs average state occupancy $\langle n \rangle$ and I_b for high and low temperatures. The experimental data and calculations are shown with open and filled symbols, respectively. The structure of S85 was used in the calculations, which were performed self-consistently for a uniaxial stress value of $\sigma_{yy} = 30$ kbars. The downward arrows indicate the locations of steps that occurred in R_p upon an increasing excitation at low temperatures for both the experimental data and calculations.

by $|j\rangle$. The Bloch part of the hole wave functions $|\psi_h\rangle$ is represented by the six basis p -like functions, $|i\rangle$, in the following representation: $|x\uparrow\rangle$, $|y\uparrow\rangle$, $|z\uparrow\rangle$, $|x\downarrow\rangle$, $|y\downarrow\rangle$, and $|z\downarrow\rangle$, where coordinates x , y , and z refer to the $[1-100]$, $[11-20]$, and $[0001]$ crystallographic directions. For the hole state l , $F_{hl,i}(\vec{r})$ are the six hole envelope functions that are obtained from the 3D 6×6 $\mathbf{k} \cdot \mathbf{p}$ method and $F_{ek,j}(\vec{r})$ are the two electron envelope functions for the electron state k obtained from the 3D single effective mass calculation. The polarization anisotropy ratio R_p is then calculated from Eq. (1) as

$$R_p = \frac{I_{\perp}}{I_{\parallel}} = \left| \frac{M_{\perp}}{M_{\parallel}} \right|^2. \quad (2)$$

Using this method, the calculated R_p is shown with filled symbols on the right of Fig. 11 for S85. The results agree qualitatively with the experimental polarized CL results for R_p , as shown with the open symbols on the left of Fig. 11. For low temperature, it is apparent that a minimal thermal excitation of the hole states results in an R_p that is roughly independent of excitation until the first electron and hole levels are doubly occupied. Upon increasing the excitation ($I_b > \sim 12$ nA), a sudden decrease in R_p is observed at low temperatures where a step is observed (downward arrows) for both the experiment and calculations in Fig. 11, consis-

tent with the participation of hole states whose relative p_x -orbital character of the Bloch states f_{xj} also decreases. In comparison, R_p decreases gradually and nearly linearly as a function of $\langle n \rangle$ for $\langle n \rangle \leq 2$ at $T=300$ K, as observed in both the experiment and calculations, owing to a continuous partial excitation of holes to higher energy hole states during the occupation of holes in the lowest lying hole levels. Thus, the theory agrees very well with the experimental results for the excitation dependence of R_p at room temperature and low temperature, as shown in Figs. 2 and 11. We attribute carrier filling and a thermal excitation of holes into higher energy hole states during excitation to account for a nearly linear decrease in R_p with $\langle n \rangle$ at $T=300$ K, while almost no thermal excitation of holes occurs at the lowest temperatures in the calculations ($T=5$ K).

V. CONCLUSION

In this work, GaN/AlN self-assembled QDs were grown by the Stranski–Krastanov method on a Si(111) substrate using molecular beam epitaxy. During the subsequent cooling from growth temperatures, the thermal expansion coefficient mismatch between the Si substrate and GaN/AlN film containing vertically stacked QDs led to an additional tensile stress at the Si/III-nitride interface, which is partially relaxed by the formation of microcracks that propagate parallel to the interface and mainly along the $\langle 11-20 \rangle$ directions. We demonstrated that these defects serve as excellent stressors, which can modify the strain tensor of QDs in close proximity (i.e., within a few microns) of the microcracks. Using CLWI we mapped the energy shifts in the QD excitonic transition energy in close proximity of the microcracks and showed that the stress perturbation leads to a blueshift of ~ 50 – 80 meV in transitioning from a pure biaxially stressed to a uniaxially stressed region. The AE for the thermal quenching of the luminescence was mapped using CL AE imaging. The AE increased from ~ 20 to 50 meV in transitioning from regions of pure biaxial to uniaxial stress and corresponds to the changes in the average AlN band edge energy, relative to the ground state QD electron and hole levels. This correspondence is consistent with the notion that defect states participating in nonradiative recombination are tied to the AlN band edges and that the thermal re-emission involves correlated e - h pairs in the thermal quenching of the luminescence in the temperature range of $240 \leq T \leq 300$ K.

The excitonic luminescence of QDs with a uniaxial stress perturbation exhibits an in-plane linear polarization anisotropy. Localized CL spectroscopy of the QDs exhibits emissions from both the ground and excited states, whose relative contributions depend on the level of excitation and temperature. We have studied these emissions using polarization-resolved CL for ensembles of QDs. The effects of screening of the polarization field in the QD, state-filling, changes in the polarization anisotropy and lifetime with varying excitation were studied experimentally with CL and theoretically with a 3D 6×6 $\mathbf{k} \cdot \mathbf{p}$ calculation method. Using the method of ensemble CL, we excited locally groups of vertically stacked QDs in varying proximity to the microcracks. The

local strain tensors for such QDs, which are subject to an interfacial stress perturbation, have been determined by modeling the dependence of the QD excitonic transition energy on the interfacial stress. Varying levels of excitation were employed by adjusting the e-beam current to analyze the effects of carrier filling in the QDs and the resulting emission from excited states. Experimental results indicate that the polarization anisotropy ratio R_p vanishes at high temperatures with an increasing excitation of the QDs, while the anisotropy decreases more slowly with excitation at low temperatures. A theoretical modeling of the effect of carrier filling on the polarization anisotropy and lifetime was performed, as based on 3D self-consistent solutions of the Schrödinger and the Poisson equations using the $6 \times 6 \mathbf{k} \cdot \mathbf{p}$ and effective mass methods for the calculation of the e - h wave functions, including the effects of the interfacial stress, microcrack-induced stress perturbation, carrier-induced screening of the QD polarization field, temperature, and occupation of the QD excited states through changes in the electron and hole quasi-Fermi levels. We attribute carrier filling and a thermal excitation of holes into higher energy hole states during excitation to account for a nearly linear decrease in the polarization anisotropy ratio R_p , with $\langle n \rangle$ at $T = 300$ K, while almost no thermal excitation of holes occurs at the lowest temperatures in the calculations ($T = 5$ K). These results demonstrate the complex interplay between external stress, temperature, and excitation conditions on the polarization dependence of the excitonic luminescence from an ensemble of GaN/AlN self-assembled QDs.

¹S. Tanaka, H. Hirayama, Y. Aoyagi, Y. Narukawa, Y. Kawakami, and S. Fujita, *Appl. Phys. Lett.* **71**, 1299 (1997).

²B. Damilano, N. Grandjean, F. Semond, J. Massies, and M. Leroux, *Appl. Phys. Lett.* **75**, 962 (1999).

³B. Damilano, N. Grandjean, J. Massies, and F. Semond, *Appl. Surf. Sci.* **164**, 241 (2000).

⁴S. Kalliakos, T. Bretagnon, P. Lefebvre, T. Taliencio, B. Gil, N. Grandjean, B. Damilano, A. Dussaigne, and J. Massies, *J. Appl. Phys.* **96**, 180 (2004).

⁵A. D. Andreev and E. P. O'Reilly, *Phys. Rev. B* **62**, 15851 (2000).

⁶A. Dadgar *et al.*, *Phys. Status Solidi C* **0**, 1583 (2003).

⁷D. Rudloff *et al.*, *Appl. Phys. Lett.* **82**, 367 (2003).

⁸G. Sarusi, O. Moshe, S. Khatsevich, D. H. Rich, and B. Damilano, *Phys. Rev. B* **75**, 075306 (2007).

⁹O. Moshe, D. H. Rich, B. Damilano, and J. Massies, *Phys. Rev. B* **77**, 155322 (2008).

¹⁰O. Moshe, D. H. Rich, B. Damilano, and J. Massies, *Phys. Status Solidi C* **6**, 1432 (2009).

¹¹B. Daudin, F. Widmann, G. Feuillet, Y. Samson, M. Arlery, and J. L. Rouviere, *Phys. Rev. B* **56**, R7069 (1997).

¹²M. Miyamura, K. Tachibana, and Y. Arakawa, *Appl. Phys. Lett.* **80**, 3937 (2002).

¹³H. T. Lin, D. H. Rich, A. Konkar, P. Chen, and A. Madhukar, *J. Appl. Phys.* **81**, 3186 (1997).

¹⁴K. Rammohan, D. H. Rich, R. S. Goldman, J. Chen, H. H. Wieder, and K. L. Kavanagh, *Appl. Phys. Lett.* **66**, 869 (1995).

¹⁵K. Rammohan, H. T. Lin, D. H. Rich, and A. Larsson, *J. Appl. Phys.* **78**, 6687 (1995).

¹⁶K. H. Lee, J. H. Na, R. A. Taylor, S. N. Yi, S. Birner, Y. S. Park, C. M. Park, and T. W. Kang, *Appl. Phys. Lett.* **89**, 023103 (2006).

¹⁷V. A. Fonoberov and A. A. Balandin, *J. Vac. Sci. Technol. B* **22**, 2190 (2004).

¹⁸I. Vurgaftman and J. R. Meyer, *J. Appl. Phys.* **94**, 3675 (2003); I. Vurgaftman, J. R. Meyer, and L. R. Ram-Mohan, *ibid.* **89**, 5815 (2001).

¹⁹O. Ambacher *et al.*, *J. Phys.: Condens. Matter* **14**, 3399 (2002).

²⁰D. P. Williams, A. D. Andreev, E. P. O'Reilly, and D. A. Faux, *Phys. Rev. B* **72**, 235318 (2005); D. P. Williams, A. D. Andreev, and E. P. O'Reilly, *ibid.* **73**, 241301 (2006).

²¹S. Khatsevich, D. H. Rich, E. T. Kim, and A. Madhukar, *J. Appl. Phys.* **97**, 123520 (2005).

²²V. Ranjan, G. Allan, C. Priester, and C. Delerue, *Phys. Rev. B* **68**, 115305 (2003).

²³J. C. Slater, *Adv. Quantum Chem.* **6**, 1 (1972).

²⁴V. A. Fonoberov and A. A. Balandin, *J. Appl. Phys.* **94**, 7178 (2003).

²⁵W. Yang, R. R. Lowe-Webb, H. Lee, and P. C. Sercel, *Phys. Rev. B* **56**, 13314 (1997).

²⁶The average carrier density is represented by $\langle n \rangle = (I_b E_b \tau L_D) / (3e E_g V_{ex} A_D)$, where L_D is the spacing between the QD layers, A_D is the areal density of the QDs, and V_{ex} is the excitation volume of the $E_b = 15$ keV electron beam. We have used $V_{ex} = 2.1 \mu\text{m}^3$ for the present GaN/AlN material system.

²⁷G. Salviati, F. Rossi, N. Armani, V. Grillo, O. Martinez, A. Vinattieri, B. Damilano, A. Matsuse, and N. Grandjean, *J. Phys.: Condens. Matter* **16**, S115 (2004).